Experimentally determined density matrices for H($n=3$) formed in H^+-He collisions from 20 to 100 keV

J. R. Ashburn, R. A. Cline, P. J. M. van der Burgt,*
W. B. Westerveld,† and J. S. Risley
Atomic Collisions Laboratory, Department of Physics, North Carolina State University, Raleigh, North Carolina 27695-8202
(Received 30 October 1989)

Density matrices describing H($n=3$) atoms produced in collisions of 20- to 100-keV protons with He atoms have been determined experimentally. In the experiment the intensity and polarization of Balmer-α radiation emitted from a He gas cell are measured as a function of the strength of an externally applied electric field. Electric fields are applied in a direction either axial to or transverse to the proton beam. Density matrices are extracted by detailed analysis of the optical data. Data are obtained for each field direction and then analyzed, separately and in combination, to yield density matrices. Satisfactory agreement is found between density matrices determined from axial and transverse electric field data except at the lowest energies studied. Some nonzero density-matrix elements are determined more accurately using axial electric fields than with transverse fields, while other elements are more accurately determined using transverse electric fields. The combined analysis using data from both field directions gives a better determination of the density matrix than the separate data sets. Results for the H($n=3$) electron-transfer cross sections (relative to 3s), the electric dipole moment of the charge distribution $\langle \mathbf{d} \rangle_z$, a first-order moment of the current distribution $\langle \mathbf{L} \times \mathbf{A} \rangle_{z,s}$, and the average coherence $\mathrm{Tr}(\underline{\sigma}_3^2)$ are obtained. The experimental results are compared to two recent calculations using the augmented atomic orbital (AO+) theory and the continuum distorted-wave approximation with post-collision interaction theory, and to one recent experimental measurement of the diagonal density-matrix elements. Both theories show qualitative agreement with the general trends in the data. The AO+ method gives better quantitative agreement. The experimental results are displayed in graphical form as distributions of the electronic charge $D(\mathbf{r})$ and of the electronic current density $\mathbf{j}(\mathbf{r})$.

I. INTRODUCTION

The study of atomic collisions has traditionally focused on the determination of cross sections for the production of particular excited states in a collision.[1] For many fundamental processes, cross sections for the dominant production channels have been measured.[2] However, in the measurement of production cross sections many details concerning the production process are averaged out. To observe a quantum-mechanically pure state, all of the parameters important in the collisional interaction must be controlled to access information about the complex scattering amplitudes. In recent years experimental emphasis has increasingly been directed toward coincidence measurements where projectiles scattered in a particular direction are measured and correlated with experimental observables relating to the reaction product(s).[3,4] Here the coherent production of energy eigenstates of a particular angular momentum has been expressed in terms of orientation and alignment parameters. The orientation is a first-order moment of the electronic current distribution of the state produced and is connected with its magnetic dipole moment; the alignment is a second-order moment of the electronic charge distribution. A special case is encountered when dealing with a hydrogenic system, where the manifold of energy eigenstates belonging to a particular principal quantum number n is nearly degenerate. In such a system quantum beats[5] or electric fields[6] can be used to measure coherences between states of different angular momentum l, some of which can be possibly of opposite parity.[7] In that case, nonzero first-order moments of the electronic charge distribution are possible, one of which is associated with an electric dipole moment.[8]

In the present paper the electron-transfer process

$$H^+ + He \rightarrow H(n=3) + He^+ \tag{1.1}$$

from 20 to 100 keV is studied. The Balmer-α radiation emitted by the decaying H($n=3$) atoms is measured as a function of externally applied electric fields. The collision process observed has axial symmetry because the measured radiation is observed regardless of impact parameter. As a consequence, only coherences between different l states are present, which are observed by Stark mixing the H($n=3$) manifold. The average H($n=3$) density matrix at the time of the electron-transfer process is derived by analysis of the optical signals. The experimentally determined H($n=3$) density matrix is, of course, just one part of the complete density matrix describing all excited states including the continuum.

The present experiment has been developed over the last several years. Preliminary results of the experiment[8,9] and an account of the analysis procedures in-

volved have been given.[10] More in depth treatments involving many significant improvements have been published since then.[11,12] A full account of the entire experiment was given in a recent publication.[13] The purpose of the present paper is to present the experimentally determined density matrices for several impact energies ranging from 20 to 100 keV.

In the range of collision energies studied neither the molecular-orbital approach nor typical high-energy approximations can reproduce the experimental results. However, comparisons made with two recent calculations[24,25] reveal the progress made in theory over the last several years. Several of the trends present in the data are reproduced in these calculation, suggesting that some of the essential features of the collisional interaction are correctly represented. However, a standing problem with these calculations is the limited range of energies to which they are applicable. No simple model of the collision is available, forcing the use of large-scale computer calculations.

The organization of this paper is as follows. First, we review the definition of the density matrix and its physical interpretation. Second, we give a brief discussion of the experimental method and analysis technique. Third, we present all of our results in tabular and graphical form and discuss the overall accuracy of our results and their general behavior.

II. THE DENSITY MATRIX AND ITS INTERPRETATION

A. The density matrix

A hydrogen atom formed in a collision between a proton and a He atom at a particular impact parameter **b** can be described by a pure state $|\Psi(\mathbf{b})\rangle$. This pure state may be expressed as a linear combination of the angular momentum eigenstates $|nlm\rangle$ with amplitudes $a_{nlm}(\mathbf{b})$,

$$|\Psi(\mathbf{b})\rangle = \sum_{n,l,m} a_{nlm}(\mathbf{b})|nlm\rangle \ . \tag{2.1}$$

In our experiment we observe H($n=3$) atoms by detecting emitted Balmer-α radiation. As a result, the summation in Eq. (2.1) is limited to $n=3$ for this experiment. Furthermore, the H($n=3$) atoms are observed regardless of impact parameter **b** so that an ensemble of H($n=3$) atoms is observed which is given by an incoherent superposition of states $|\Psi(\mathbf{b})\rangle$ for all impact parameters **b**. Because this ensemble is not in a pure state it is convenient to use a density matrix[14] $\underline{\sigma}_3$ to describe the production of the H($n=3$) atoms.

The elements of the density matrix $\underline{\sigma}_3$ follow from Eq. (2.1) as

$$\sigma_{lm;l'm'} = \int_0^{2\pi}\int_0^{\infty} a_{lm}(\mathbf{b})a^*_{l'm'}(\mathbf{b})b\ db\ d\phi \ , \tag{2.2}$$

where the amplitudes $a_{lm}(\mathbf{b})$ refer to H($n=3$) states. The density matrix $\underline{\sigma}_3$ has certain elements that are either identical to each other or zero because of symmetries in the collision. Consequently, the 9×9 H($n=3$) density matrix $\underline{\sigma}_3$ shown in Fig. 1 has only 14 independent real parameters.[10] This density matrix contains all of the information obtainable from our experiment about the production of H($n=3$) atoms.

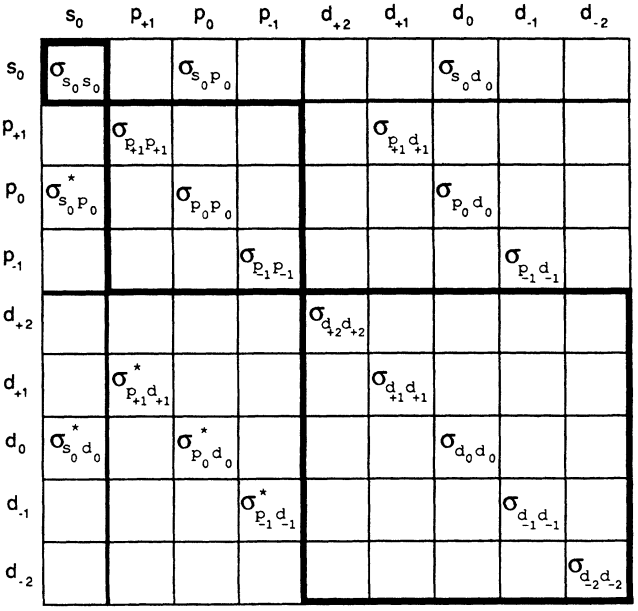

FIG. 1. Axially symmetric H($n=3$) density matrix $\underline{\sigma}_3$. The positions left blank are identically zero for reasons of symmetry.

By definition of the density matrix, certain constraints apply to the various nonzero density matrix elements. First, diagonal elements cannot be negative, $\sigma_{lm;lm} \geq 0$, and second, the magnitude of the off-diagonal elements is limited by the magnitudes of the corresponding diagonal elements according to the Schwarz inequality,[15] $|\sigma_{lm;l'm'}| \leq (\sigma_{lm;lm}\sigma_{l'm';l'm'})^{1/2}$.

B. Interpretation of the density matrix

The density matrix $\underline{\sigma}_3$ contains all the physically accessible information pertaining to the observed H($n=3$) atoms. Through suitable normalization, the diagonal elements can be identified as the cross sections for electron transfer into the various angular momentum states $|lm\rangle$. Submatrices of $\underline{\sigma}_3$ belonging to a particular angular momentum l can be characterized by their state multipole moments, such as the orientation vector and the alignment tensor. These moments can be expressed as expectation values of operators constructed out of various combinations of the angular momentum operator **L**.[16] Because of axial symmetry with respect to the incoming proton beam in this experiment, only the expectation values of the z component of these operators can be nonzero. In addition, because of reflection symmetry for planes through the z axis, the z component of the orientation vector has an expectation value which is also zero, so that no orientation is found for the ensemble studied here. Similarly, for submatrices of $\underline{\sigma}_3$ of mixed angular momentum, multipole moments have been defined[17,18] which in turn can be identified as the expectation values of suitably constructed operators. Such operators could be generated in terms of the **r** and **p** operators. However,

in the present case of a hydrogenic system it is more natural to use operators related to the constants of the motion of the system,[19] i.e., the angular momentum operator **L** and the Runge-Lenz operator **A**.[20]

The complete information contained in the density matrix can be expressed in the associated electronic charge density distribution $D(r)$ and current density distribution[9] $\mathbf{j}(\mathbf{r})$. For an axially symmetric collision these two functions can be plotted to provide a complete graphical representation of the average H($n=3$) atom at the time of production. The functions $D(\mathbf{r})$ and $\mathbf{j}(\mathbf{r})$ together depend on all the density-matrix elements.

The charge density as a function of $\mathbf{r}$ is given by

$$D(\mathbf{r})=\frac{\langle \mathbf{r}|\underline{\sigma}_3|\mathbf{r}\rangle}{\mathrm{Tr}(\underline{\sigma}_3)} = \sum_{\substack{l,m\\ l',m'}} \frac{\mathrm{Re}[\sigma_{lm;l'm'}\psi^*_{l'm'}(\mathbf{r})\psi_{lm}(\mathbf{r})]}{\mathrm{Tr}(\underline{\sigma}_3)} , \tag{2.3}$$

where $\psi_{lm}(\mathbf{r})$ are the angular momentum eigenfunctions for H($n=3$). Using this definition of $D(\mathbf{r})$, the Liouville equation can be used to obtain the current density as

$$\mathbf{j}(\mathbf{r})=\frac{\langle \mathbf{r}|v\underline{\sigma}_3|\mathbf{r}\rangle+\langle \mathbf{r}|\underline{\sigma}_3 v|\mathbf{r}\rangle}{2\,\mathrm{Tr}(\underline{\sigma}_3)} = \frac{\hbar}{m_e}\sum_{\substack{l,m\\ l',m'}} \frac{\mathrm{Im}[\sigma_{lm;l'm'}\psi^*_{l'm'}(\mathbf{r})\nabla\psi_{lm}(\mathbf{r})]}{\mathrm{Tr}(\underline{\sigma}_3)} , \tag{2.4}$$

where v is the velocity operator

$$v=\frac{\hbar}{im_e}\nabla . \tag{2.5}$$

A hydrodynamical-type relationship between $D(\mathbf{r})$ and $\mathbf{j}(\mathbf{r})$ can be derived,

$$\frac{d}{dt}D(\mathbf{r})=-\nabla\cdot\mathbf{j}(\mathbf{r}) . \tag{2.6}$$

Moments of these two distributions $D(\mathbf{r})$ and $\mathbf{j}(\mathbf{r})$ are related to the state multipoles of the density matrix $\underline{\sigma}_3$. That part of the density matrix which determines the electronic-charge-density distribution is invariant under time reversal whereas the electronic-current-density distribution is connected with the part of $\underline{\sigma}_3$ which changes sign under time reversal.[17–19]

In the following the Condon-Shortley phase convention is used for the spherical harmonics for the H($n=3$) eigenfunctions and the radial functions are defined to be positive near the origin.

A first-order moment of $D(\mathbf{r})$ is the average electric dipole moment $\langle \mathbf{d}\rangle_z$, which for the H($n=3$) density matrix is given by[8]

$$\langle \mathbf{d}\rangle_z=\frac{1}{\mathrm{Tr}(\underline{\sigma}_3)}\mathrm{Re}(6\sqrt{6}\sigma_{s_0p_0}+6\sqrt{3}\sigma_{p_0d_0}+18\sigma_{p_{\pm1}d_{\pm1}})ea_0 . \tag{2.7}$$

A positive value for $\langle \mathbf{d}\rangle_z$ indicates that the electron lags behind the proton and a negative value indicates the electron leads the proton. The largest allowable value for $\langle \mathbf{d}\rangle_z$ for H($n=3$) is $7.35ea_0$.

A first-order moment of $\mathbf{j}(\mathbf{r})$ is generated by the angular momentum operator **L**, giving the orientation vector of the ensemble. However, because of the symmetry in the experiment the orientation is identically zero. A nonzero first-order moment of $\mathbf{j}(\mathbf{r})$ is given by[9,19]

$$\langle \mathbf{L}\times\mathbf{A}\rangle_{z,s}=-\frac{1}{\mathrm{Tr}(\underline{\sigma}_3)}4\left[\frac{2}{3}\right]^{1/2}\mathrm{Im}(\sigma_{s_0p_0}+\sqrt{2}\sigma_{p_0d_0}+\sqrt{6}\sigma_{p_{\pm1}d_{\pm1}})\hbar^2 , \tag{2.8}$$

which, classically, points along the direction of the orbital velocity at the perihelion of the electron's orbit. $\langle \mathbf{L}\times\mathbf{A}\rangle_{z,s}$ is a measure of the current flow in the z direction at large distances from the z axis. The largest allowable value for $\langle \mathbf{L}\times\mathbf{A}\rangle_{z,s}$ for H($n=3$) is $2.31\hbar^2$.

The average coherence $\mathrm{Tr}(\underline{\sigma}_3^2)$, where $\mathrm{Tr}(\underline{\sigma}_3)=1$, is a measure of how closely the density matrix describes a pure state. If the collision process produces most of the atoms in the same state regardless of the impact parameter, then the average coherence will be high. If the atoms produced at different impact parameters are in different states, then $\mathrm{Tr}(\underline{\sigma}_3^2)$ will be small. For H($n=3$) this quantity varies between $\frac{1}{9}$, a completely incoherent state, and unity, a pure state. Because the $3s$ electron-transfer channel becomes more and more dominant at higher energies, the average coherence reaches a high value at the higher energies probed in the experiment. Consequently, the average coherence at higher energies is largely a measure of the dominance of the $3s$ term.

More detailed information can be obtained by parametrizing the off-diagonal density-matrix elements in terms of the corresponding diagonal elements, as

$$R_{ij}=\frac{|\sigma_{ij}|}{(\sigma_{ii}\sigma_{jj})^{1/2}} \tag{2.9}$$

and

$$\phi_{ij}=\tan^{-1}\left[\frac{\mathrm{Im}\sigma_{ij}}{\mathrm{Re}\sigma_{ij}}\right] , \tag{2.10}$$

where R_{ij} is a positive constant ($0\le R_{ij}\le 1$) and ϕ_{ij} is the phase angle of the off-diagonal element ($-180°<\phi_{ij}\le 180°$). We will refer to the quantity R_{ij} as the coherence parameter of the off-diagonal element σ_{ij}. For a fully coherent ensemble, $R_{ij}=1$ for all i,j and the following relationship holds for the phase angles:

$$\phi_{ij}+\phi_{jk}=\phi_{ik} . \tag{2.11}$$

In the experiment we are dealing with an incoherent ensemble of atoms produced over a range of impact parameters $\mathbf{b}$ over which the complex amplitudes $a_{lm}(\mathbf{b})$ vary in magnitude and phase. As a consequence, the R_{ij} values are less than unity and the phase relationship in Eq. (2.11) breaks down. However, by considering the R_{ij} and ϕ_{ij} values as a function of impact energy, certain con-

TABLE I. H($n=3$) density matrix from a 20-keV proton-helium collision normalized to the 3s cross section. Results from axial and transverse measurements are shown separately, as well as results from combined fitting of axial and transverse data (see text for explanation of combined χ^2).

Element	Axial	Transverse	Combined
s_0	1.00±0.16	1.00±0.14	1.000±0.082
p_0	1.92±0.11	1.42±0.21	1.784±0.060
$p_{\pm1}$	0.811±0.057	0.600±0.055	0.740±0.037
d_0	0.38±0.23	0.40±0.14	0.576±0.077
$d_{\pm1}$	0.28±0.16	0.21±0.10	0.130±0.055
$d_{\pm2}$	−0.002±0.042	0.011±0.027	0.034±0.013
Re(s_0p_0)	0.37±0.18	−0.40±0.32	0.373±0.090
Im(s_0p_0)	30±23	−0.26±0.10	−0.283±0.086
Re(s_0d_0)	−0.20±0.34	−0.05±0.30	0.14±0.11
Im(s_0d_0)	−0.4±1.4	−0.9±1.1	−0.29±0.46
Re(p_0d_0)	0.943±0.088	0.425±0.085	0.800±0.032
Im(p_0d_0)	−0.079±0.084	−0.166±0.057	−0.090±0.029
Re($p_{\pm1}d_{\pm1}$)	0.26±0.10	0.333±0.043	0.291±0.031
Im($p_{\pm1}d_{\pm1}$)	−0.141±0.098	−0.058±0.013	−0.038±0.012
$\langle \mathbf{d} \rangle_z$	3.65±0.31	1.0±1.1	3.68±0.21
$\langle \mathbf{L}\times\mathbf{A} \rangle_{z,s}$	−17±14	0.465±0.099	0.319±0.054
Tr($\underline{\sigma}_3^2$)	59±90	0.34±0.19	0.297±0.021
χ^2	2.19	7.29	1.13

clusions can be drawn about the impact parameter dependence of the collision process.

III. EXPERIMENTAL METHOD

A detailed description of the experiment and the analysis of measured signals has been given elsewhere.[13] Only a brief discussion is given here. A proton beam passes through a helium gas cell and excited H atoms are produced all along the beam. Balmer-α radiation from H($n=3$) atoms is detected from a section of the beam and the radiation is analyzed for its polarization characteristics by measuring the Stokes parameters.[21] Static electric fields are applied in the gas cell either axial to or transverse to the proton beam direction. The applied electric fields Stark mix the H($n=3$) manifold, affect the time evolution of the atoms, and consequently affect the intensity and polarization of the emitted light. From an analysis of the measured electric field dependence of the Stokes parameters we extract the density matrix for the

TABLE II. H($n=3$) density matrix from a 25-keV proton-helium collision normalized to the 3s cross section. Results from axial and transverse measurements are shown separately, as well as results from combined fitting of axial and transverse data (see text for explanation of combined χ^2).

Element	Axial	Transverse	Combined
s_0	1.000±0.059	1.000±0.041	1.000±0.024
p_0	1.384±0.043	1.119±0.058	1.223±0.018
$p_{\pm1}$	0.288±0.020	0.269±0.015	0.269±0.010
d_0	0.177±0.089	0.178±0.038	0.204±0.021
$d_{\pm1}$	0.067±0.061	0.073±0.027	0.049±0.015
$d_{\pm2}$	0.013±0.016	0.005±0.007	0.013±0.004
Re(s_0p_0)	0.512±0.059	0.372±0.076	0.484±0.026
Im(s_0p_0)	7.4±5.7	−0.477±0.028	−0.497±0.023
Re(s_0d_0)	0.03±0.12	0.173±0.068	0.158±0.030
Im(s_0d_0)	−1.14±0.47	0.16±0.26	−0.13±0.11
Re(p_0d_0)	0.479±0.025	0.380±0.022	0.425±0.009
Im(p_0d_0)	−0.073±0.023	−0.064±0.015	−0.067±0.008
Re($p_{\pm1}d_{\pm1}$)	0.121±0.031	0.131±0.011	0.124±0.008
Im($p_{\pm1}d_{\pm1}$)	−0.005±0.031	0.007±0.004	0.013±0.003
$\langle \mathbf{d} \rangle_z$	4.45±0.17	3.93±0.38	4.46±0.10
$\langle \mathbf{L}\times\mathbf{A} \rangle_{z,s}$	−7.3±5.6	0.603±0.038	0.593±0.025
Tr($\underline{\sigma}_3^2$)	11±16	0.408±0.021	0.437±0.008
χ^2	2.42	2.75	1.05

TABLE III. H($n=3$) density matrix from a 30-keV proton-helium collision normalized to the 3s cross section. Results from axial and transverse measurements are shown separately, as well as results from combined fitting of axial and transverse data (see text for explanation of combined χ^2).

Element	Axial	Transverse	Combined
s_0	1.000±0.040	1.000±0.028	1.000±0.017
p_0	0.797±0.028	0.780±0.036	0.757±0.011
$p_{\pm1}$	0.122±0.012	0.102±0.009	0.113±0.006
d_0	0.051±0.057	0.080±0.020	0.088±0.013
$d_{\pm1}$	0.040±0.040	0.028±0.015	0.019±0.009
$d_{\pm2}$	0.004±0.011	0.010±0.004	0.010±0.002
$\mathrm{Re}(s_0p_0)$	0.490±0.032	0.473±0.058	0.456±0.018
$\mathrm{Im}(s_0p_0)$	1.1±2.8	−0.404±0.021	−0.410±0.017
$\mathrm{Re}(s_0d_0)$	0.049±0.082	0.102±0.038	0.143±0.019
$\mathrm{Im}(s_0d_0)$	−0.43±0.29	−0.26±0.17	−0.230±0.061
$\mathrm{Re}(p_0d_0)$	0.240±0.014	0.212±0.017	0.218±0.006
$\mathrm{Im}(p_0d_0)$	−0.023±0.013	−0.012±0.010	−0.021±0.005
$\mathrm{Re}(p_{\pm1}d_{\pm1})$	0.031±0.017	0.055±0.008	0.050±0.006
$\mathrm{Im}(p_{\pm1}d_{\pm1})$	0.009±0.019	0.007±0.003	0.009±0.002
$\langle\mathbf{d}\rangle_z$	4.71±0.14	4.74±0.040	4.63±0.10
$\langle\mathbf{L}\times\mathbf{A}\rangle_{z,s}$	−1.7±4.2	0.615±0.040	0.642±0.027
$\mathrm{Tr}(\underline{\sigma}_3^2)$	1.1±2.7	0.582±0.043	0.576±0.014
χ^2	2.69	2.15	1.07

average H($n=3$) atom at the time of its production.

Because of symmetries only 14 independent parameters are needed to completely specify the axially symmetric H($n=3$) density matrix. Characteristic optical signals or fitting functions (Stokes parameters as a function of applied electric field) are calculated numerically for each density-matrix element. The experimentally measured optical signals are linear superpositions of these characteristic signals, with 14 independent parameters needed to specify the density matrix as coefficients. In calculating the fitting functions the spatial variation of the electric field and the target density are accounted for. Corrections for cascade from $n=4$ are made by calculating characteristic optical signals for each H($n=4$) density-matrix element[22] and using theoretically calculated values of the H($n=4$) density-matrix elements.[23] The 14 coefficients are extracted through linear statistical fitting of the characteristic signals to the measured data.

TABLE IV. H($n=3$) density matrix from a 35-keV proton-helium collision normalized to the 3s cross section. Results from axial and transverse measurements are shown separately, as well as results from combined fitting of axial and transverse data (see text for explanation of combined χ^2).

Element	Axial	Transverse	Combined
s_0	1.000±0.026	1.000±0.019	1.000±0.011
p_0	0.548±0.018	0.536±0.026	0.546±0.007
$p_{\pm1}$	0.070±0.007	0.063±0.007	0.066±0.004
d_0	0.062±0.037	0.052±0.016	0.061±0.009
$d_{\pm1}$	0.003±0.026	0.015±0.012	0.006±0.007
$d_{\pm2}$	0.009±0.007	0.009±0.003	0.010±0.002
$\mathrm{Re}(s_0p_0)$	0.468±0.020	0.397±0.031	0.433±0.011
$\mathrm{Im}(s_0p_0)$	1.1±1.3	−0.334±0.013	−0.329±0.011
$\mathrm{Re}(s_0d_0)$	0.134±0.052	0.141±0.027	0.157±0.012
$\mathrm{Im}(s_0d_0)$	−0.20±0.18	−0.27±0.10	−0.230±0.038
$\mathrm{Re}(p_0d_0)$	0.158±0.008	0.131±0.010	0.145±0.004
$\mathrm{Im}(p_0d_0)$	0.013±0.008	0.003±0.006	0.008±0.003
$\mathrm{Re}(p_{\pm1}d_{\pm1})$	0.002±0.010	0.030±0.005	0.023±0.004
$\mathrm{Im}(p_{\pm1}d_{\pm1})$	0.000±0.010	0.008±0.002	0.008±0.001
$\langle\mathbf{d}\rangle_z$	4.83±0.11	4.39±0.26	4.686±0.077
$\langle\mathbf{L}\times\mathbf{A}\rangle_{z,s}$	−2.1±2.4	0.575±0.028	0.551±0.020
$\mathrm{Tr}(\underline{\sigma}_3^2)$	1.4±1.9	0.665±0.041	0.671±0.012
χ^2	2.26	2.39	1.01

TABLE V. H($n=3$) density matrix from a 40-keV proton-helium collision normalized to the 3s cross section. Results from axial and transverse measurements are shown separately, as well as results from combined fitting of axial and transverse data (see text for explanation of combined χ^2).

Element	Axial	Transverse	Combined
s_0	1.000±0.017	1.000±0.013	1.000±0.008
p_0	0.415±0.012	0.415±0.018	0.417±0.005
$p_{\pm1}$	0.051±0.005	0.024±0.005	0.034±0.003
d_0	0.036±0.024	0.049±0.011	0.051±0.006
$d_{\pm1}$	0.008±0.017	−0.002±0.008	−0.003±0.005
$d_{\pm2}$	0.006±0.005	0.013±0.002	0.012±0.001
Re(s_0p_0)	0.416±0.011	0.383±0.018	0.397±0.007
Im(s_0p_0)	−1.58±0.81	−0.252±0.009	−0.247±0.007
Re(s_0d_0)	0.099±0.032	0.098±0.018	0.129±0.008
Im(s_0d_0)	−0.11±0.11	−0.219±0.067	−0.142±0.025
Re(p_0d_0)	0.099±0.005	0.094±0.006	0.097±0.003
Im(p_0d_0)	0.020±0.005	0.019±0.004	0.022±0.002
Re($p_{\pm1}d_{\pm1}$)	0.011±0.006	0.017±0.004	0.014±0.002
Im($p_{\pm1}d_{\pm1}$)	0.008±0.007	0.006±0.001	0.005±0.001
$\langle \mathbf{d} \rangle_z$	4.645±0.073	4.50±0.18	4.570±0.057
$\langle \mathbf{L}\times\mathbf{A} \rangle_{z,s}$	3.2±1.6	0.446±0.021	0.429±0.016
Tr($\underline{\sigma}_3^2$)	2.6±2.0	0.736±0.030	0.710±0.008
χ^2	1.30	1.58	1.11

In addition, by properly propagating the statistical errors in the statistical fitting procedure the covariance matrix of the 14 parameters is obtained. Quantities like the electric dipole moment which depend on several of these 14 parameters can be computed, including their error estimates, from the 14 coefficients and corresponding covariance matrices.

Consistency checks can be applied to the experimentally determined density matrices. First, the physical constraints discussed in Sec. II must be satisfied, i.e., diagonal elements must be positive and off-diagonal elements must obey the Schwarz inequality. Second, separate analysis of the optical data obtained from axial and transverse electric field measurements must yield agreement between the extracted density matrices. These comparisons serve as indicators of possible systematic errors not accounted for in the analysis.

IV. RESULTS AND DISCUSSION

A. Precision of the measurements

Tables I–IX show our experimental results for the nine collision energies studied. The tables show density-matrix elements determined separately from axial and transverse electric field measurements as well as a com-

TABLE VI. H($n=3$) density matrix from a 50-keV proton-helium collision normalized to the 3s cross section. Results from axial and transverse measurements are shown separately, as well as results from combined fitting of axial and transverse data (see text for explanation of combined χ^2).

Element	Axial	Transverse	Combined
s_0	1.000±0.016	1.000±0.012	1.000±0.007
p_0	0.261±0.011	0.250±0.017	0.282±0.005
$p_{\pm1}$	0.030±0.005	0.008±0.004	0.013±0.003
d_0	0.025±0.024	0.019±0.010	0.030±0.006
$d_{\pm1}$	0.005±0.017	0.008±0.007	−0.001±0.005
$d_{\pm2}$	0.005±0.004	0.009±0.002	0.011±0.001
Re(s_0p_0)	0.361±0.010	0.354±0.012	0.355±0.006
Im(s_0p_0)	−0.69±0.57	−0.138±0.007	−0.132±0.006
Re(s_0d_0)	0.091±0.031	0.070±0.019	0.090±0.008
Im(s_0d_0)	0.019±0.093	−0.278±0.055	−0.154±0.024
Re(p_0d_0)	0.055±0.004	0.065±0.005	0.057±0.002
Im(p_0d_0)	0.038±0.005	0.032±0.004	0.026±0.002
Re($p_{\pm1}d_{\pm1}$)	0.005±0.005	0.003±0.002	0.004±0.002
Im($p_{\pm1}d_{\pm1}$)	0.018±0.007	0.003±0.001	0.002±0.001
$\langle \mathbf{d} \rangle_z$	4.367±0.075	4.50±0.15	4.333±0.058
$\langle \mathbf{L}\times\mathbf{A} \rangle_{z,s}$	1.4±1.3	0.210±0.017	0.219±0.015
Tr($\underline{\sigma}_3^2$)	1.24±0.85	0.875±0.040	0.782±0.009
χ^2	1.45	1.21	1.29

TABLE VII. H($n=3$) density matrix from a 60-keV proton-helium collision normalized to the $3s$ cross section. Results from axial and transverse measurements are shown separately, as well as results from combined fitting of axial and transverse data (see text for explanation of combined χ^2).

Element	Axial	Transverse	Combined
s_0	1.000±0.015	1.000±0.015	1.000±0.008
p_0	0.209±0.011	0.170±0.020	0.213±0.005
$p_{\pm1}$	0.024±0.004	0.002±0.005	0.007±0.003
d_0	0.013±0.021	0.026±0.012	0.030±0.007
$d_{\pm1}$	0.006±0.015	0.003±0.009	−0.005±0.005
$d_{\pm2}$	0.004±0.004	0.011±0.002	0.011±0.001
$\mathrm{Re}(s_0p_0)$	0.332±0.009	0.297±0.011	0.324±0.006
$\mathrm{Im}(s_0p_0)$	0.42±0.52	−0.067±0.009	−0.061±0.007
$\mathrm{Re}(s_0d_0)$	0.072±0.029	0.052±0.023	0.105±0.009
$\mathrm{Im}(s_0d_0)$	−0.095±0.085	−0.212±0.059	−0.090±0.026
$\mathrm{Re}(p_0d_0)$	0.044±0.004	0.043±0.006	0.042±0.002
$\mathrm{Im}(p_0d_0)$	0.012±0.004	0.025±0.005	0.019±0.002
$\mathrm{Re}(p_{\pm1}d_{\pm1})$	0.000±0.004	0.002±0.002	0.000±0.002
$\mathrm{Im}(p_{\pm1}d_{\pm1})$	−0.004±0.006	0.001±0.001	0.002±0.001
$\langle\mathbf{d}\rangle_z$	4.138±0.075	3.94±0.16	4.106±0.060
$\langle\mathbf{L}\times\mathbf{A}\rangle_{z,s}$	−1.1±1.3	0.072±0.020	0.073±0.017
$\mathrm{Tr}(\underline{\sigma}_3^2)$	0.99±0.52	0.872±0.040	0.813±0.008
χ^2	1.65	1.74	1.30

bined analysis using data from both field directions. Each density matrix has been normalized to the s_0 element. Diagonal elements are displayed as $p_{\pm1}=p_{+1}=p_{-1}$ and off-diagonal elements are taken from the upper triangle of the matrix. The reduced χ^2 value from the statistical fit is also shown. In the combined analysis, data sets from axial and transverse electric field directions were weighted by their respective $1/\chi^2$ values before being combined in the fit. The resulting χ^2 for the combined fit should, therefore, be near unity. The error bars shown for each density-matrix element have been multiplied by $(\chi^2)^{1/2}$ to give a more accurate estimate for the precision of the measurement.

To check the validity of our measurements we test our results for positive diagonal elements and the Schwarz inequality. An examination of all of the measured density matrices shows satisfactory agreement with these two requirements within the experimental uncertainty. This agreement indicates only that the measured density matrices are physically realistic. It does not guarantee that they are correct.

As a further check, density matrices extracted sepa-

TABLE VIII. H($n=3$) density matrix from an 80-keV proton-helium collision normalized to the $3s$ cross section. Results from axial and transverse measurements are shown separately, as well as results from combined fitting of axial and transverse data (see text for explanation of combined χ^2).

Element	Axial	Transverse	Combined
s_0	1.000±0.029	1.000±0.015	1.000±0.010
p_0	0.159±0.020	0.136±0.019	0.164±0.006
$p_{\pm1}$	0.016±0.006	0.007±0.005	0.005±0.003
d_0	0.038±0.036	0.004±0.011	0.027±0.008
$d_{\pm1}$	−0.015±0.026	0.012±0.008	−0.007±0.006
$d_{\pm2}$	0.009±0.007	0.007±0.002	0.011±0.001
$\mathrm{Re}(s_0p_0)$	0.266±0.013	0.266±0.009	0.267±0.008
$\mathrm{Im}(s_0p_0)$	−0.32±0.59	0.013±0.009	0.019±0.007
$\mathrm{Re}(s_0d_0)$	0.054±0.045	0.079±0.021	0.063±0.010
$\mathrm{Im}(s_0d_0)$	0.05±0.15	−0.129±0.050	−0.057±0.028
$\mathrm{Re}(p_0d_0)$	0.025±0.007	0.031±0.005	0.025±0.002
$\mathrm{Im}(p_0d_0)$	0.014±0.008	0.024±0.004	0.015±0.002
$\mathrm{Re}(p_{\pm1}d_{\pm1})$	0.005±0.007	0.005±0.002	0.003±0.002
$\mathrm{Im}(p_{\pm1}d_{\pm1})$	0.014±0.009	0.003±0.001	0.003±0.001
$\langle\mathbf{d}\rangle_z$	3.50±0.13	3.62±0.14	3.500±0.087
$\langle\mathbf{L}\times\mathbf{A}\rangle_{z,s}$	0.7±1.5	−0.153±0.019	−0.128±0.019
$\mathrm{Tr}(\underline{\sigma}_3^2)$	0.94±0.51	0.852±0.027	0.811±0.010
χ^2	1.25	1.69	1.21

TABLE IX. H($n=3$) density matrix from a 100-keV proton-helium collision normalized to the $3s$ cross section. Results from axial and transverse measurements are shown separately, as well as results from combined fitting of axial and transverse data (see text for explanation of combined χ^2).

Element	Axial	Transverse	Combined
s_0	1.000±0.020	1.000±0.017	1.000±0.009
p_0	0.127±0.015	0.149±0.024	0.153±0.005
$p_{\pm1}$	0.013±0.004	−0.006±0.007	0.003±0.003
d_0	−0.023±0.027	−0.003±0.013	0.027±0.007
$d_{\pm1}$	0.026±0.020	0.011±0.009	−0.009±0.005
$d_{\pm2}$	−0.001±0.005	0.010±0.003	0.012±0.001
$\mathrm{Re}(s_0p_0)$	0.239±0.010	0.224±0.012	0.241±0.007
$\mathrm{Im}(s_0p_0)$	0.32±0.31	0.058±0.012	0.072±0.007
$\mathrm{Re}(s_0d_0)$	−0.021±0.030	0.069±0.023	0.054±0.009
$\mathrm{Im}(s_0d_0)$	0.059±0.088	−0.081±0.048	−0.052±0.021
$\mathrm{Re}(p_0d_0)$	0.025±0.004	0.027±0.007	0.021±0.002
$\mathrm{Im}(p_0d_0)$	0.005±0.005	0.024±0.006	0.011±0.002
$\mathrm{Re}(p_{\pm1}d_{\pm1})$	−0.005±0.004	0.006±0.003	−0.001±0.002
$\mathrm{Im}(p_{\pm1}d_{\pm1})$	−0.002±0.006	0.005±0.002	0.003±0.001
$\langle \mathbf{d} \rangle_z$	3.118±0.089	3.13±0.17	3.143±0.069
$\langle \mathbf{L}\times\mathbf{A} \rangle_{z,s}$	−0.90±0.83	−0.286±0.024	−0.259±0.020
$\mathrm{Tr}(\underline{\sigma}_3^2)$	0.97±0.29	0.836±0.023	0.818±0.010
χ^2	1.64	1.75	1.23

rately from axial and transverse field measurements can be compared. Comparison reveals that some of the density-matrix elements do not agree between the axial and transverse determinations to within the experimental uncertainty. In particular, the results for the $p_{\pm1}$ element disagree at the higher proton energies and the results for the $\mathrm{Re}(s_0p_0)$ and $\mathrm{Im}(s_0p_0)$ elements disagree at lower energies. In most cases the disagreement is only slightly outside of the error bars, indicating that based on statistics the error estimates are too low. At lower energies, however, we note that the values of χ^2 become larger, especially for transverse measurements, possibly indicating an energy-dependent systematic effect influencing primarily the transverse field measurements. Because of the large values of χ^2 for the lowest energies, these results should be viewed with caution. For most density-matrix elements, agreement between axial and transverse determinations indicates the absence of large systematic effects in the experiment since it is unlikely that axial and transverse measurements would be affected in the same way by systematic effects. The relative agreement between the axial and transverse determinations is indicated by the value of χ^2 from the combined fit. Since χ^2 is not unity, the axial and transverse are in disagreement. However, since χ^2 never exceeds 1.3 for the combined fit, we conclude that our measurements are of sufficient quality to warrant a comparison with available theoretical results.

From a comparison of the size of the error bars from axial and transverse determinations it is seen that some density-matrix elements are better determined by one field direction than by the other. For example, p_0 and $\mathrm{Re}(s_0p_0)$ are better determined using axial fields while s_0, d_0, $d_{\pm1}$, $d_{\pm2}$, and the imaginary terms are better determined using transverse fields. Since axial and transverse field measurements complement each other, the com-

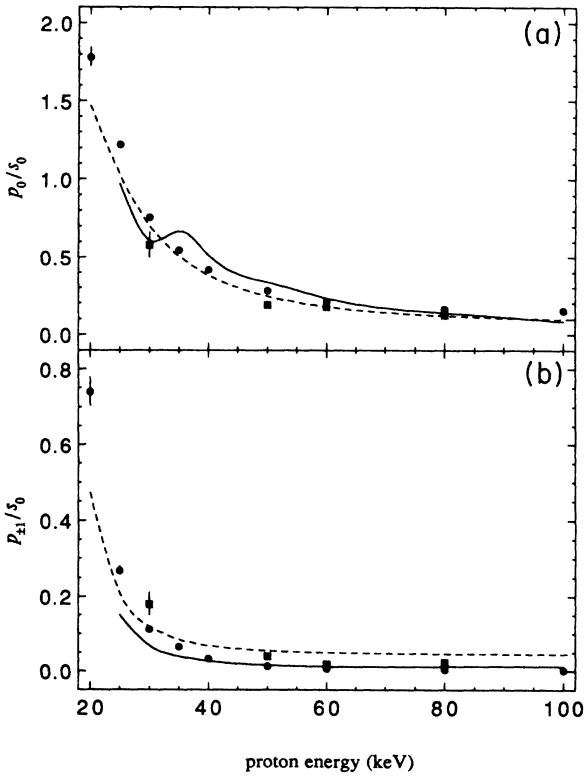

FIG. 2. H($n=3$) electron-transfer cross sections relative to s_0 as a function of impact energy: (a) p_0; (b) $p_{\pm1}$. Present results, ●; Brower and Pipkin (Ref. 27), ■; AO+ (Ref. 24), ——; continuum distorted-wave approximation with post-collision interaction (CDW-PCI) (Ref. 25); — — —. The theoretical calculations were performed at discrete energies and then connected by a smooth curve.

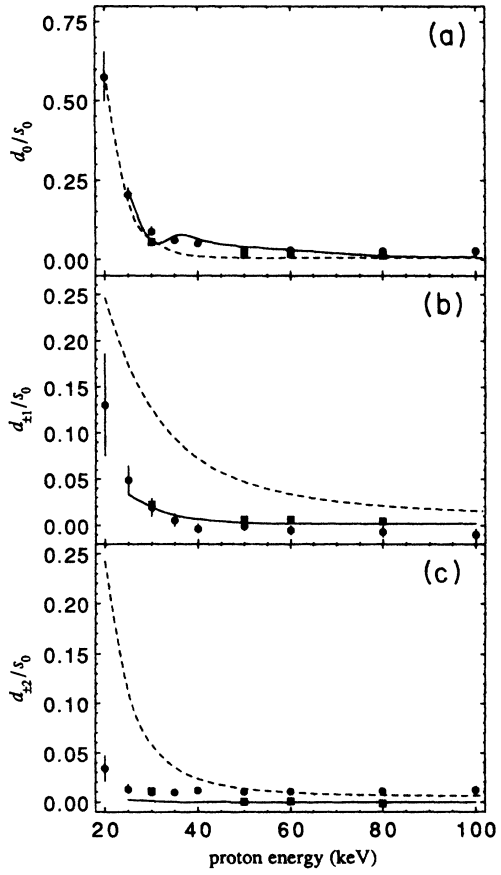

FIG. 3. H($n=3$) electron-transfer cross sections relative to s_0 as a function of impact energy: (a) d_0; (b) $d_{\pm1}$; (c) $d_{\pm2}$. Symbols as given in Fig. 2.

bined analysis using data from both field directions should be less sensitive to systematic effects which cause disagreements between axial and transverse results. In fact, for some density-matrix elements the combined result is outside of the range given by the axial and transverse results. This indicates that the combined analysis is not simply an average of the axial and transverse results but a more sensitive determination of the density-matrix elements.

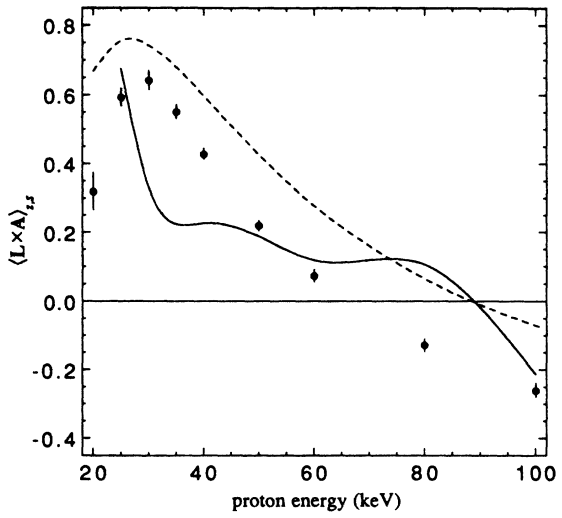

FIG. 5. $\langle \mathbf{L}\times\mathbf{A}\rangle_{z,s}$ moment as a function of impact energy. Symbols as given in Fig. 2.

In general, in the combined analysis of data taken from both electric field directions some density-matrix elements are determined to better precision than others. The most precisely determined elements are the real and imaginary parts of the p-d off-diagonal terms followed by the diagonal terms and next $\mathrm{Re}(s_0p_0)$ and $\mathrm{Im}(s_0p_0)$. The least-well-determined elements are the $\mathrm{Re}(s_0d_0)$ and $\mathrm{Im}(s_0d_0)$ elements. For some of the smaller elements, the uncertainties are larger than the values.

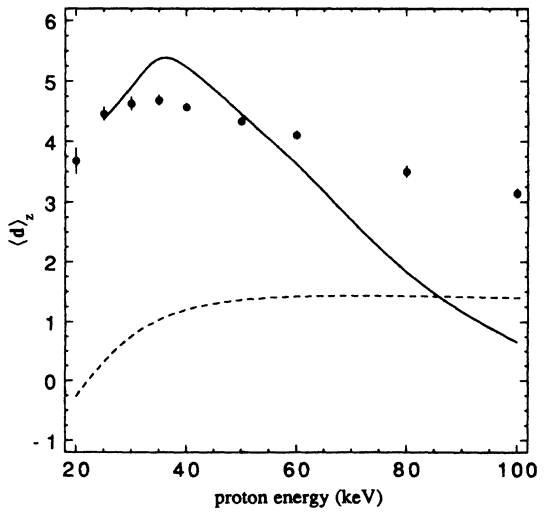

FIG. 4. Electric dipole moment $\langle \mathbf{d}\rangle_z$ as a function of impact energy. Symbols as given in Fig. 2.

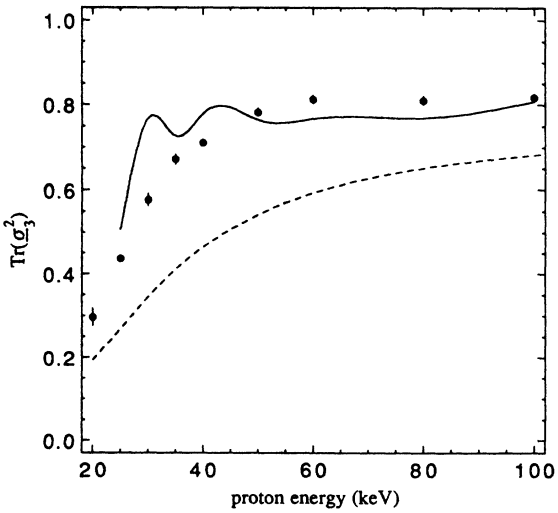

FIG. 6. Average coherence $\mathrm{Tr}(\underline{\sigma}_3^2)$ as a function of impact energy. Symbols as given in Fig. 2.

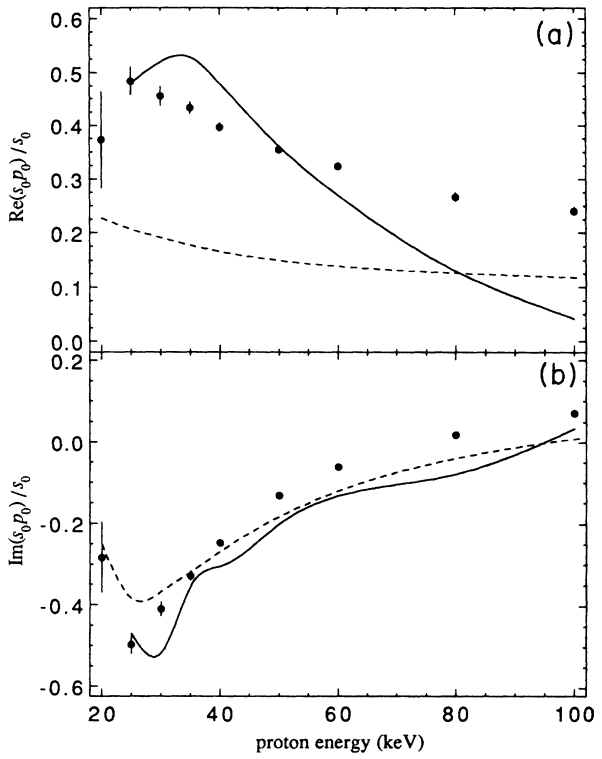

FIG. 7. Off-diagonal elements relative to s_0 as a function of impact energy: (a) $\mathrm{Re}(s_0p_0)$; (b) $\mathrm{Im}(s_0p_0)$. Symbols as given in Fig. 2.

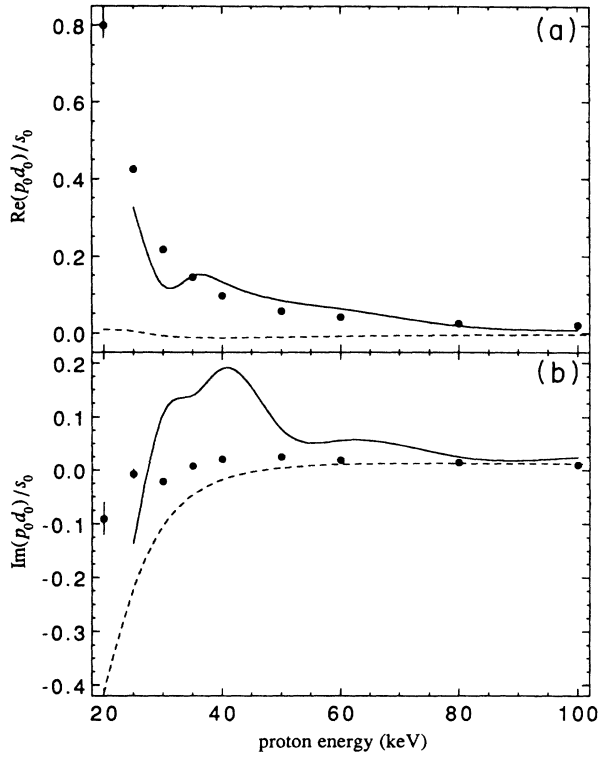

FIG. 9. Off-diagonal elements relative to s_0 as a function of impact energy: (a) $\mathrm{Re}(p_0d_0)$; (b) $\mathrm{Im}(p_0d_0)$. Symbols as given in Fig. 2.

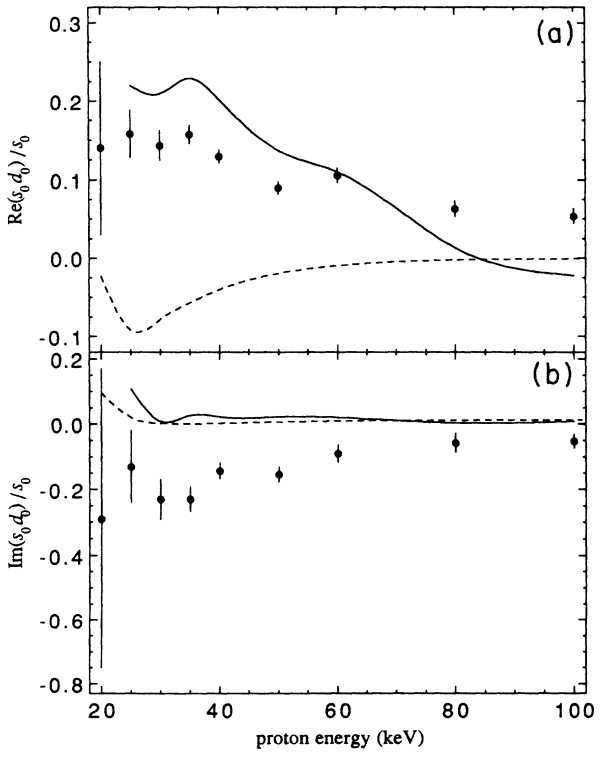

FIG. 8. Off-diagonal elements relative to s_0 as a function of impact energy: (a) $\mathrm{Re}(s_0p_0)$; (b) $\mathrm{Im}(s_0p_0)$. Symbols as given in Fig. 2.

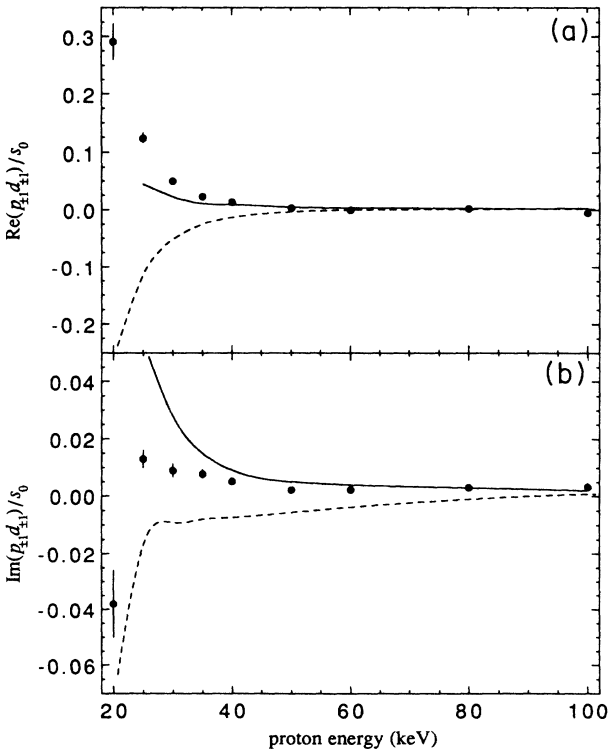

FIG. 10. Off-diagonal elements relative to s_0 as a function of impact energy: (a) $\mathrm{Re}(p_{\pm1}d_{\pm1})$; (b) $\mathrm{Im}(p_{\pm1}d_{\pm1})$. Symbols as given in Fig. 2.

B. General trends in the results

Individual density-matrix elements and linear combinations of physical significance are shown graphically in Figs. 2–12. In these graphs experimental results obtained from the combined analysis are shown along with results from theoretical calculations by Jain, Lin, and Fritsch[24] and by Dubé.[25] The calculations by Jain, Lin and Fritsch[24] use the augmented atomic orbital (AO+) method, a modified two-center atomic-orbital expansion in which the regular atomic-orbital basis is supplemented by pseudostates which are designed to model molecular effects at lower energies and excitation and ionization channels at higher energies. The calculations by Dubé[25] use the continuum distorted-wave approximation[26] (CDW), which is an extension of the first and second Born approximations that includes multiple-scattering contributions. This treatment also includes contributions from final-state interactions (PCI) due to Stark mixing of the nearly degenerate hydrogenic levels in the Coulomb field of the receding target ion. The calculations shown here use Hartree-Fock wave functions for the He atom.

In Figs. 2 and 3 the diagonal elements of the density matrix normalized to $3s$ at each energy are shown. These figures also include measurements by Brower and Pipkin,[27] who determine the electron-transfer cross sections to individual magnetic sublevels of $H(n=3)$ using a microwave-resonance, optical-detection technique. In this technique transitions within the $H(n=3)$ manifold are driven by a microwave field and changes in Balmer-α intensity are measured to determine the electron-transfer cross sections. Only diagonal elements of the $H(n=3)$ density matrix are obtained from this experimental method.

All of the diagonal elements (relative to $3s$) decrease with increasing proton energy (see Figs. 2 and 3). The calculations in the AO+ and continuum distorted-wave approximation with post-collision interaction (CDW-PCI) schemes reproduce this behavior of the diagonal terms and almost agree to within experimental uncertainties with the present results, except for $d_{\pm1}$ and $d_{\pm2}$. Comparing our results with the experimental results of Brower and Pipkin,[27] we see that the results mostly do not agree to within the quoted error bars. For p_0 Brower and Pipkin's results are consistently somewhat lower, while their $p_{\pm1}$ results are always higher than the present

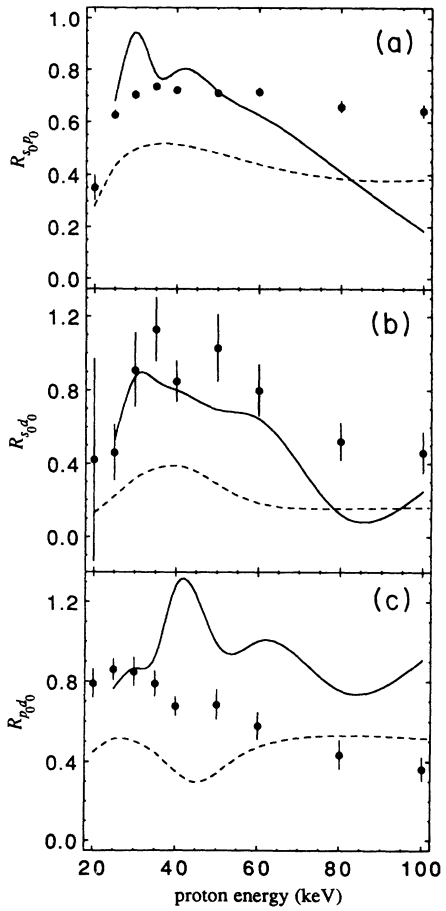

FIG. 11. Coherence parameters R_{ij} as a function of impact energy: (a) $R_{s_0p_0}$; (b) $R_{s_0d_0}$; (c) $R_{p_0d_0}$. Symbols as given in Fig. 2.

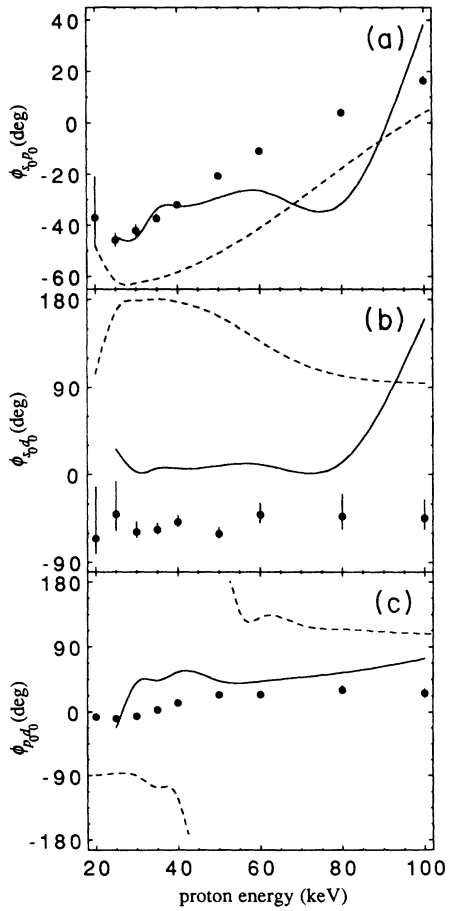

FIG. 12. Phase angles ϕ_{ij} as a function of impact energy (a) $\phi_{s_0p_0}$; (b) $\phi_{s_0d_0}$; (c) $\phi_{p_0d_0}$. Symbols as given in Fig. 2.

results. A similar behavior is also true for the d_0 and the $d_{\pm 1}$ results. However, the overall trends in Brower and Pipkin's results agree well with the present results.

The results for the dipole moment of the electronic density distribution $\langle \mathbf{d} \rangle_z$, shown in Fig. 4, indicate that the AO+ calculation is more successful than the CDW-PCI in the energy range shown. However, at higher energies the results of the AO+ calculation do not follow the experimental results, probably indicating that more states should be included in the basis set for the ionization channels. Since the first Born approximation predicts purely imaginary off-diagonal terms, it is not surprising that the CDW-PCI calculation gives a poor estimate for the electric dipole moment.

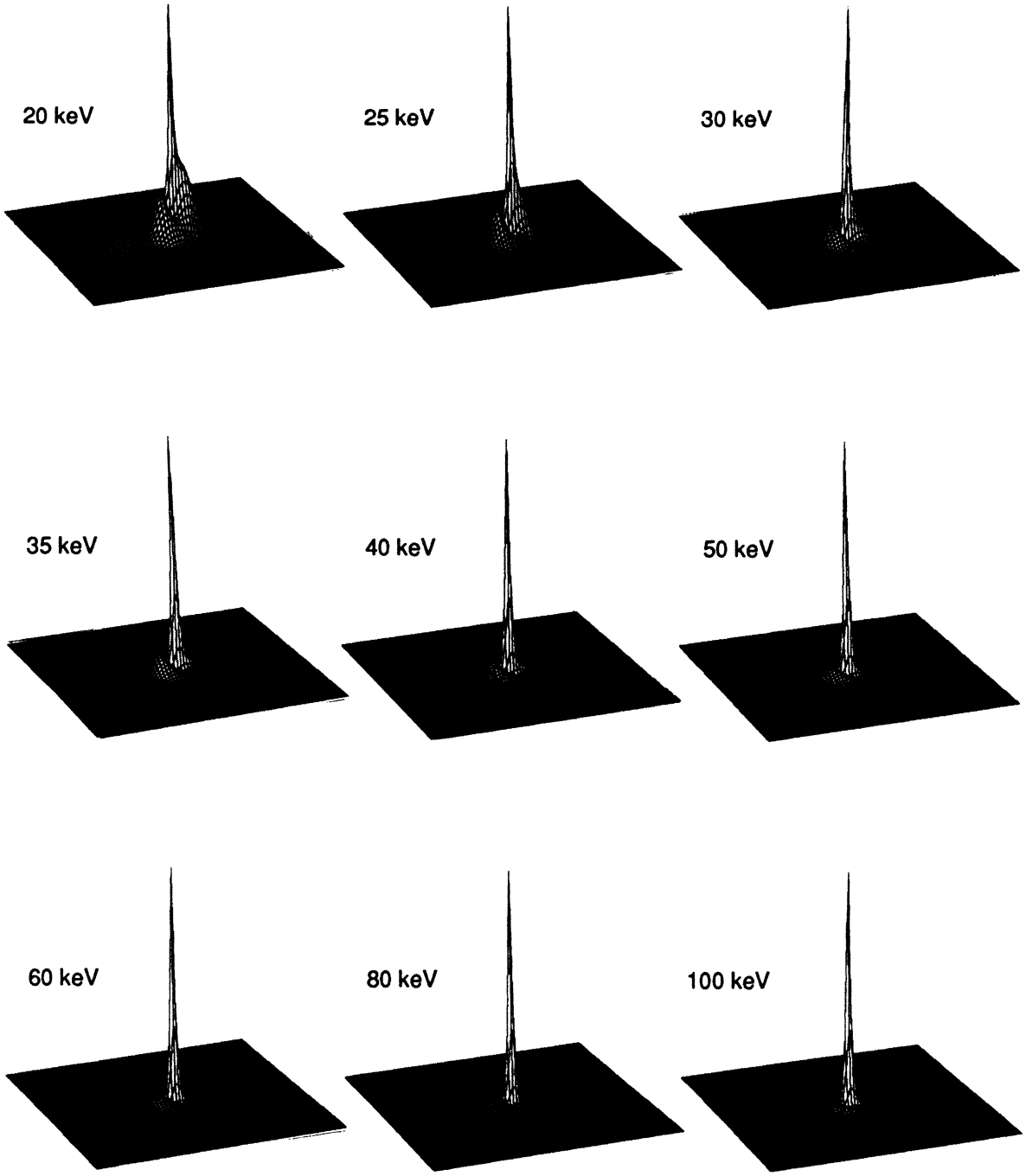

FIG. 13. Charge density distribution $D(\mathbf{r})$ in the x-z plane. $D(\mathbf{r})$ is indicated by height. In this figure the H atom is traveling to the right and the recoil He^+ ion is far to the left. The range shown is from $-20a_0$ to $20a_0$ and the grid size is $0.5a_0$.

The results for a first-order moment of the electronic-current-density distribution $\langle \mathbf{L}\times\mathbf{A}\rangle_{z,s}$ are shown in Fig. 5. In this case the CDW-PCI theory is much better in predicting $\langle \mathbf{L}\times\mathbf{A}\rangle_{z,s}$ than in predicting $\langle \mathbf{d}\rangle_z$. In fact, it is somewhat more successful than the AO+ calculation in predicting the location and magnitude of the maximum and the zero crossing point. The AO+ calculation does not indicate a clear maximum. The AO+ calculation also does not predict a smooth variation with energy.

Figure 6 shows that the average coherence increases at higher energies. This result stems from the fact that at higher energies the $3s$ element is increasingly dominant. At energies less than 30 keV, however, the p_0 cross section is larger than the s_0. The low coherence of the pro-

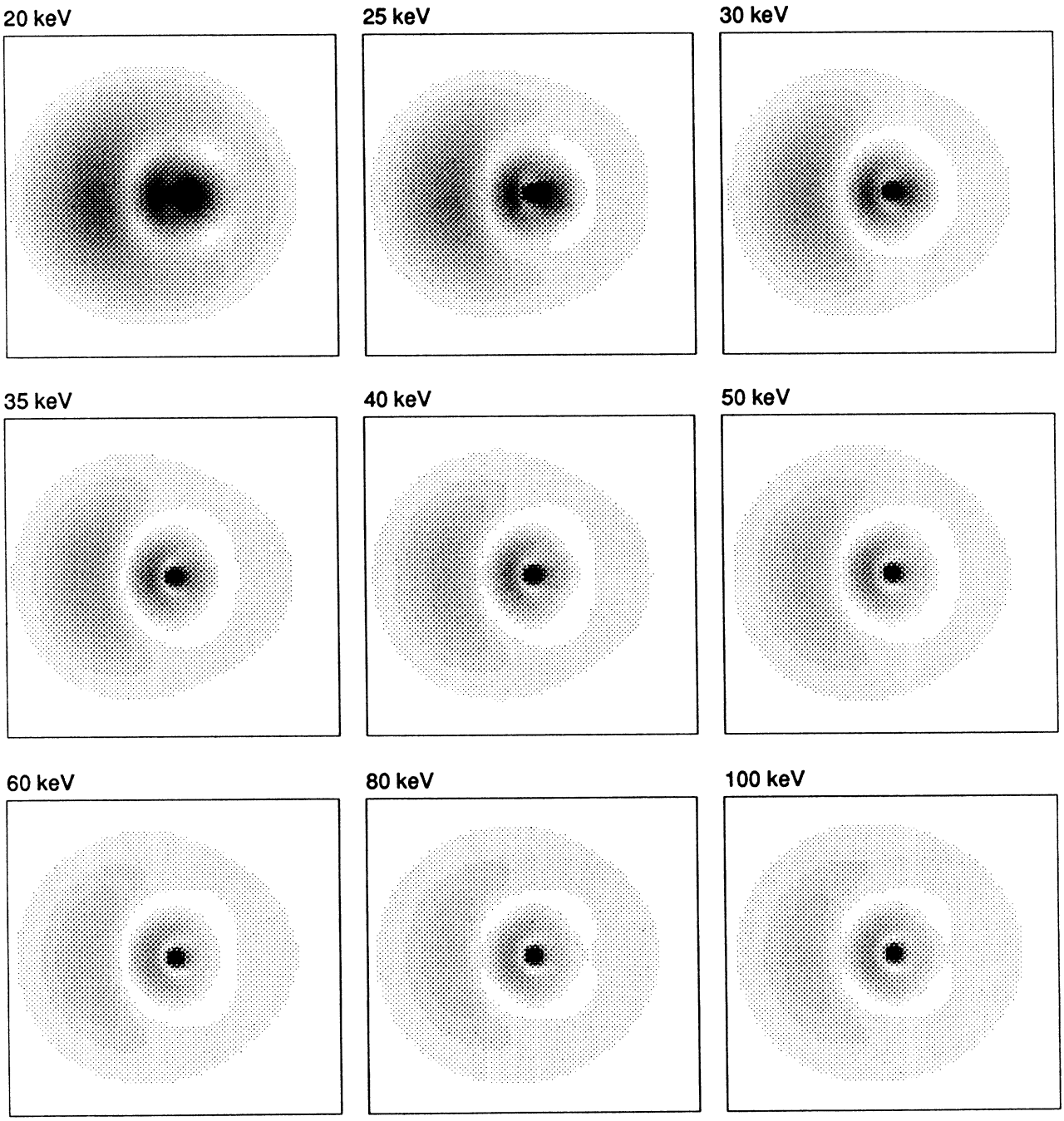

FIG. 14. Charge density distribution $D(\mathbf{r})$ in the x-z plane. $D(\mathbf{r})$ is indicated by shading. In this figure the H atom is traveling to the right and the recoil He^+ ion is far to the left. The box indicates the range from $-20a_0$ to $20a_0$.

duced average H($n=3$) atoms is an indication of a substantial variation of the complex production amplitudes and, especially, their phases as a function of impact parameter. The AO+ result exhibits an oscillatory behavior of the coherence as a function of energy, in contrast to the CDW-PCI result. However, CDW-PCI consistently underestimates the experimental coherence.

The behavior of the off-diagonal elements is shown and compared with calculations in Figs. 7–10. At high energies, some elements have large fractional uncertainties because their values are so small compared to the dominant $3s$ element. In general, the AO+ calculation shows better agreement for the real parts than does the CDW-PCI calculation.

In Figs. 11 and 12 off-diagonal terms are plotted in parametrized form giving the coherence parameters R_{ij} and phase angles ϕ_{ij} from Eqs. (2.9) and (2.10). $R_{p_{\pm1}d_{\pm1}}$ and $\phi_{p_{\pm1}d_{\pm1}}$ are not shown because their error bars are too large to show discernible trends. Discernible trends are clearly observed for the s_0p_0 and p_0d_0 off-diagonal terms. Theoretical predictions show poor agreement except for the most dominant terms. The coherence parameter for the s_0p_0 element is quite large except for the lower energies studied. The behavior at the lower energies can possibly be understood as a consequence of the increasing importance of molecular effects. In direct contrast stands the behavior of the p_0d_0 coherence parameter which shows a steady decrease toward higher energies. This could be an indication that, at higher energies,

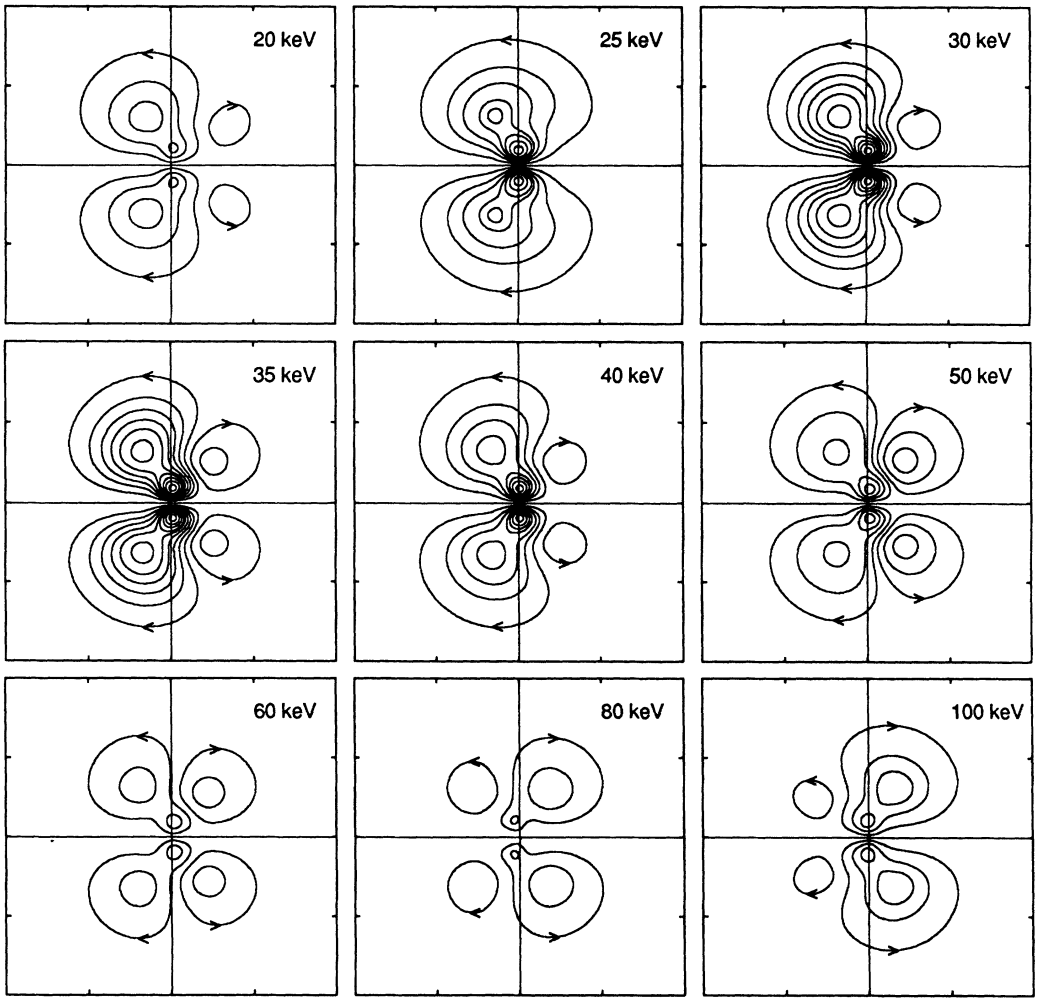

FIG. 15. Current density distribution $\mathbf{j}(\mathbf{r})$ in the x-z plane. As in Figs. 13 and 14, the H atom is traveling to the right. The box indicates the range from $-20a_0$ to $20a_0$. There is an equal amount of current flow between adjacent flow lines so that the density of flow lines indicates the magnitude of the current density. The presentation of the three-dimensional flow pattern in a plane such that the density of flow lines represents the magnitude of flow is realized through weighting of the current vectors $\mathbf{j}(\mathbf{r})$ by the distance to the z axis, taking advantage of the axial symmetry.

the s_0 and p_0 excitation have a similar impact parameter dependence which differs from that of the d_0 excitation. The phase angles for the s_0p_0 and the p_0d_0 off-diagonal elements show very similar behavior. No relationship of the kind given in Eq. (2.11) seems to be valid here when comparing with the s_0d_0 phase, except possibly at the lower energies where a rather high coherence exists for all the off-diagonal terms.

In Figs. 13 and 14 the charge density distributions $D(\mathbf{r})$ are shown for the collision energies studied. These pictures clearly indicate that the electric dipole moment is largest around 35 keV and that the electron lags behind the proton. Figure 15 displays the current density distributions $\mathbf{j}(\mathbf{r})$. In these pictures the behavior of $\langle \mathbf{L}\times\mathbf{A}\rangle_{z,s}$ can be seen. Near 30 keV the number of current density curves is the largest, indicating a large current flow. Between 60 and 80 keV the change in direction of $\mathbf{j}(\mathbf{r})$ at large distances from the z axis is consistent with the change of sign in $\langle \mathbf{L}\times\mathbf{A}\rangle_{z,s}$.

ACKNOWLEDGMENTS

The authors gratefully acknowledge stimulating conversations with Chii-Dong Lin, Ashok Jain, Louis Dubé, and Eugen Merzbacher. We also thank Ashok Jain and Louis Dubé for making their unpublished results available to us. The characteristic optical signals were calculated using an FPS-264 processor at the Cornell National Supercomputer Facility, a resource of the Cornell Theory Center, which is funded in part by the National Science Foundation, New York State, the IBM Corporation, and members of the Center's Corporate Research Institute. This work was supported in part by the Atomic, Molecular and Plasma Physics Program of the National Science Foundation, under Grant No. PHY-88-09083.

*Present address: Department of Physics, University of Windsor, Windsor, Ontario, Canada.

†Permanent address: Department of Physics, University of Utrecht, Utrecht, The Netherlands.

[1]E. W. Thomas, *Excitation in Heavy Particle Collisions* (Wiley, New York, 1972).

[2]J. E. Bayfield, in *Atomic Physics*, edited by G. zu Putlitz, E. W. Weber, and A. Winnacker (Plenum, New York, 1975), Vol. 4, p. 397.

[3]Joseph Macek and D. H. Jaecks, Phys. Rev. A **4**, 2288 (1971).

[4]J. F. Williams, Indian J. Phys. B **62**, 235 (1988).

[5]Robert DeSerio, Carlos Gonzalez-Lepera, John P. Gibbons, Joachim Burgdörfer, and I. A. Sellin, Phys. Rev. A **37**, 4111 (1988).

[6]R. Krotkov, Phys. Rev. A **12**, 1793 (1975).

[7]T. G. Eck, Phys. Rev. Lett. **31**, 270 (1973).

[8]C. C. Havener, W. B. Westerveld, J. S. Risley, N. H. Tolk, and J. C. Tully, Phys. Rev. Lett. **48**, 926 (1982).

[9]C. C. Havener, N. Rouze, W. B. Westerveld, and J. S. Risley, Phys. Rev. Lett. **53**, 1049 (1984).

[10]C. C. Havener, N. Rouze, W. B. Westerveld, and J. S. Risley, Phys. Rev. A **33**, 276 (1986).

[11]W. B. Westerveld, J. R. Ashburn, R. A. Cline, C. D. Stone, P. J. M. van der Burgt, and J. S. Risley, Nucl. Instrum. Methods B **24/25**, 224 (1987).

[12]W. B. Westerveld, J. R. Ashburn, R. A. Cline, C. D. Stone, P. J. M. van der Burgt, and J. S. Risley, in *Correlation and Polarization in Electronic and Atomic Collisions*, edited by Albert Crowe and Michael R. H. Rudge (World Scientific, Singapore, 1988), pp. 271–302.

[13]J. R. Ashburn, R. A. Cline, C. D. Stone, P. J. M. van der Burgt, W. B. Westerveld, and J. S. Risley, Phys. Rev. A **40**, 4885 (1989).

[14]Karl Blum, *Density Matrix Theory and Applications* (Plenum, New York, 1981).

[15]Eugen Merzbacher, *Quantum Mechanics* (Wiley, New York, 1970), p. 168.

[16]U. Fano and Joseph H. Macek, Rev. Mod. Phys. **45**, 553 (1973).

[17]Gerald Gabrielse, Phys. Rev. A **22**, 138 (1980).

[18]A. Omont, Prog. Quantum Electron. **5**, 69 (1977).

[19]Joachim Burgdörfer, Z. Phys. A **309**, 285 (1983).

[20]L. C. Biedenharn and J. D. Louck, *Angular Momentum in Quantum Physics* (Addison-Wesley, London, 1981), pp. 335–362.

[21]D. Clarke and J. F. Grainger, *Polarized Light and Optical Measurement* (Pergamon, Oxford, 1971), pp. 35–39.

[22]J. R. Ashburn, Ph.D. thesis, North Carolina State University, 1989.

[23]Ashok Jain (private communication).

[24]Ashok Jain, C. D. Lin, and W. Fritsch, Phys. Rev. A **35**, 3180 (1987); **36**, 2041 (1987); **37**, 3611(E) (1988).

[25]Louis Dubé (private communication).

[26]Joachim Burgdörfer and Louis J. Dubé, Nucl. Instrum. Methods B **10/11**, 198 (1985); Phys. Rev. Lett. **52**, 2225 (1984).

[27]M. C. Brower and F. M. Pipkin, Phys. Rev. A **39**, 3323 (1989).

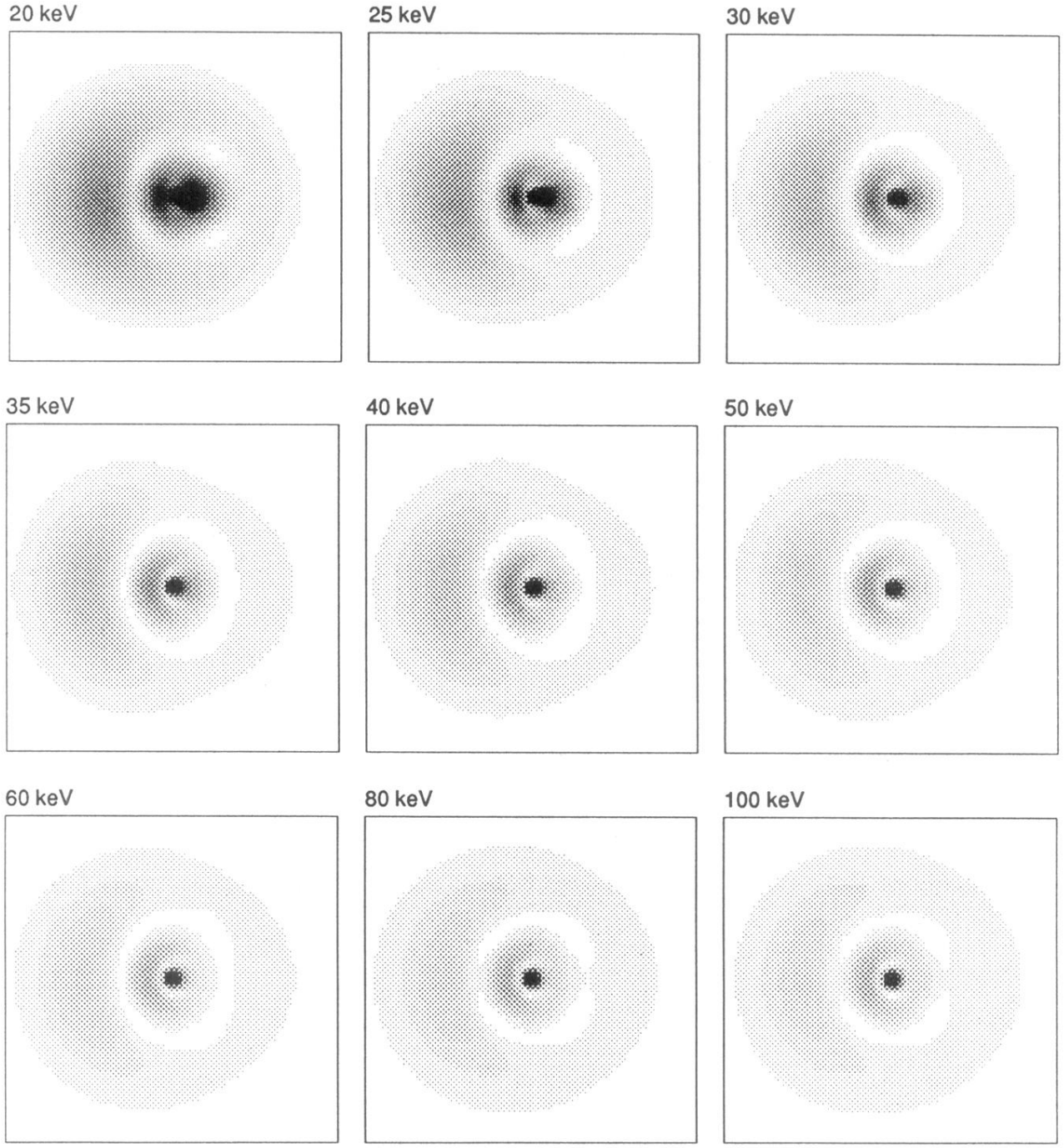

FIG. 14. Charge density distribution $D(\mathbf{r})$ in the x-z plane. $D(\mathbf{r})$ is indicated by shading. In this figure the H atom is traveling to the right and the recoil He^+ ion is far to the left. The box indicates the range from $-20a_0$ to $20a_0$.